Astronomy & Astrophysics manuscript no. AGN˙LF˙and˙Biasing
April 15, 2013

Linking X-ray AGN with dark matter halos: a model compatible with AGN luminosity function and large-scale clustering properties

Gert Hütsi[1,2], Marat Gilfanov[1,3], Rashid Sunyaev[1,3]

[1] Max-Planck-Institut für Astrophysik, Karl-Schwarzschild-Str. 1, 85741 Garching, Germany
e-mail: gert@mpa-garching.mpg.de
[2] Tartu Observatory, Tõravere 61602, Estonia
[3] Space Research Institute of Russian Academy of Sciences, Profsoyuznaya 84/32, 117997 Moscow, Russia

Received / Accepted

ABSTRACT

Aims. Our goal is to find a minimalistic model describing the luminosity function and large-scale clustering bias of the X-ray selected AGN in the general framework of the concordance ΛCDM model.
Methods. We assume that a simple population-averaged scaling relation between the AGN X-ray luminosity $L_{\rm X}$ and the host dark matter halo mass $M_{\rm h}$ exists. With such a relation, the AGN X-ray luminosity function can be computed from the halo mass function. Using for the latter the concordance ΛCDM halo mass function, we obtain the $M_{\rm h} - L_{\rm X}$ relation required to match the redshift dependent AGN X-ray luminosity function known from X-ray observations.
Results. We find that with a simple power law scaling $M_{\rm h} \propto L_{\rm X}^{\Gamma(z)}$, our model can successfully reproduce the observed X-ray luminosity function. Furthermore, we automatically obtain predictions for the large-scale AGN clustering amplitudes and their dependence on the luminosity and redshift, which seem to be compatible with AGN clustering measurements. Our model also includes the redshift-dependent AGN duty cycle which peaks at the redshift $z \simeq 1$ and its peak value is consistent with unity, suggesting that on average there is no more than one AGN per dark matter halo. For a typical X-ray selected AGN at $z \sim 1$, our best-fit $M_{\rm h} - L_{\rm X}$ scaling implies low Eddington ratio $L_{\rm X}/L_{\rm Edd} \sim 10^{-4} - 10^{-3}$ and correspondingly large mass growth e-folding times, suggesting that the typical X-ray AGN are dominantly fueled via relatively inefficient 'hot-halo' accretion mode.

Key words. Galaxies: active – X-rays: galaxies – Cosmology: theory – large-scale structure of Universe

1. Introduction

A realization that every galaxy of significant size harbors a supermassive black hole (SMBH) (with masses $\sim 10^6 - 10^9\,M_\odot$) is probably one of the most remarkable discoveries of modern astrophysics. The growth of SMBHs, as manifested by the active galactic nuclei (AGN), has been observed over a broad range of electromagnetic energies, from radio to hard X-rays and gamma-rays. The observed AGN X-ray emission, believed to originate from the upscattering of softer accretion disk photons via inverse Compton mechanism by the hot electron corona, has proven to be the most effective way of selecting large samples of AGN over large cosmological volumes [1]. This efficiency owes to the fact that in order to absorb X-rays one needs significant column densities of absorbing material, which is particularly true in the hard X-ray band, where $N_{\rm H} \sim 10^{24}$ cm^{-2} is required.

With XMM-Newton [2] and Chandra [3] X-ray observatories, two of the most advanced X-ray instruments in existence, more than 20 deep extragalactic X-ray surveys over varying sky areas and limiting sensitivities have been performed (Brandt & Hasinger 2005). The most noticeable amongst these are ∼ 2 Ms Chandra Deep Field North (Alexander et al. 2003) over ≃ 448 arcmin^2 sky area, ∼ 4 Ms Chandra Deep Field South (Xue et al. 2011) over ≃ 465 arcmin^2, and ∼ 3 Ms XMM-Newton deep survey covering Chandra Deep Field South (Comastri et al. 2011).

Despite the small sky areas covered by those deep surveys, a relatively large number of detected AGN has allowed reasonably good determination of the AGN luminosity function (LF) and its evolution over cosmic time (Ueda et al. 2003; Hasinger et al. 2005; Aird et al. 2010). Even though these narrow survey geometries are not very suitable for measuring the spatial clustering properties of AGN, somewhat wider and shallower surveys like X-Boötes, XMM-LSS, AEGIS, and XMM-COSMOS have allowed measurement of the two-point clustering statistics (Murray et al. 2005; Gandhi et al. 2006; Coil et al. 2009; Gilli et al. 2009; Allevato et al. 2011), albeit with relatively large uncertainty on large scales. The large-scale clustering measurements are expected to improve significantly with the upcoming Spectrum-X-Gamma/eROSITA [4] [5] space mission (Predehl et al. 2010), which is planned to cover entire sky down to the limiting sensitivity of ∼ 10^{-14} erg/s/cm^2 in the $0.5 - 2$ keV band (Merloni et al. 2012; Kolodzig et al. 2012).

[1] In comparison, the deepest optical spectroscopic surveys typically give a factor of ∼ 10 times less AGN per deg^{-2}, and only utradeep optical variability studies are able to generate comparable AGN sky densities (e.g., Brandt & Hasinger 2005).
[2] http://xmm.esac.esa.int
[3] http://chandra.harvard.edu
[4] http://www.mpe.mpg.de/erosita/
[5] http://hea.iki.rssi.ru/SRG/

Even though the evolution of AGN over cosmic time is an interesting subject on its own, the remarkable discoveries of correlations between SMBH masses and host galaxy properties (see, e.g., Kormendy & Richstone 1995; Ferrarese & Ford 2005, for reviews), hinting for the underlying AGN-galaxy co-evolution mechanisms, have significantly broadened the importance and actuality of those topics in astronomical community. Although controversial in terms of observational data (e.g., Ferrarese 2002; Kormendy & Bender 2011), in currently favored cold dark matter (CDM) cosmologies, where the structure grows in a hierarchical fashion starting from the smallest scales (i.e., the bottom-up scenario), it is quite natural that SMBH masses $M_{\rm BH}$ should also (at least up to some level) correlate with the masses of the host dark matter halos $M_{\rm h}$. Indeed, this is what one quite commonly finds in semi-analytic AGN-galaxy co-evolution models, e.g. Fanidakis et al. (2012). Despite the fact that there is a significant scatter in the $M_{\rm BH}$-$M_{\rm h}$ relation, hinting that there are other important parameters beyond $M_{\rm h}$ (and possibly one needs a full merger history) that determine $M_{\rm BH}$, it is still reasonable to use $M_{\rm h}$ as a single proxy for $M_{\rm BH}$, this way linking $M_{\rm BH}$ to the quantities we have currently good theoretical predictions available, i.e., halo mass function (MF) and clustering bias.

Future wide field X-ray surveys like eROSITA promise to give us very precise AGN clustering bias parameters as a function of redshift and luminosity (Kolodzig et al. 2013). Since clustering bias provides direct information on how AGN populate dark matter halos, this also helps in determining, e.g., the dominant X-ray AGN fuelling mode: 'hot halo' *vs* 'cold gas' accretion. As an example, semi-analytic models of Fanidakis et al. (2012) suggest for the hot halo fuelling mode quite strong dependence between the AGN X-ray luminosity and host halo mass, with brighter AGN populating preferentially higher mass (and thus more strongly biased) halos. For the cold gas accretion, on the other hand, which is presumably responsible for most of the quasar activity, the host halo mass and AGN luminosity are only weakly dependent, with most of the activity occurring in somewhat lower mass halos.

In this paper we assume that there exists a relation between the dark matter halo mass and the AGN X-ray luminosity it harbors, and therefore, the X-ray luminosity function of AGN can be computed from the mass function of dark matter halos. The search for the functional form of this relation consistent with the concordance ΛCDM halo mass function and the observed X-ray AGN LF is presented in Section 2. It turns out that this way we indeed obtain acceptable fit to the X-ray AGN LF and, as a bonus, automatically obtain a prediction about X-ray AGN clustering properties, which seems to agree with available observational data. This and other consequences of our simple model is given in Section 3. We bring our conclusions in Section 4.

Throughout this paper we assume a flat ΛCDM cosmology with $\Omega_{\rm m} = 0.27$, $\Omega_{\rm b} = 0.045$, $h = 0.70$ and $\sigma_8 = 0.80$.

2. Mapping halo MF to X-ray AGN LF

AGN luminosity can be parameterized via the Eddington ratio

$$L_{\rm X} = f_{\rm Edd} L_{\rm Edd} \propto f_{\rm Edd} M_{\rm BH} \qquad (1)$$

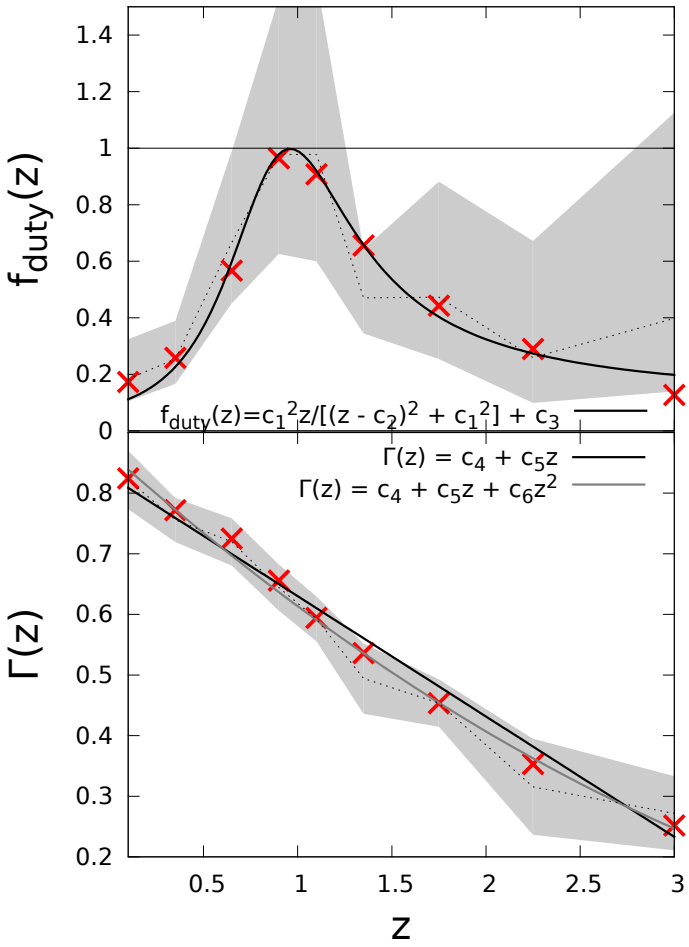

Fig. 1. Best fitting duty cycle values $f_{\rm duty}(z_i)$ (*upper panel*) and power law indices $\Gamma(z_i)$ from Eq. (2) (*lower panel*) in nine redshift bins, shown with red crosses. In the *upper panel* the power law index is assumed to be in parametric form $\Gamma(z) = c_4 + c_5 z$ while the amplitude factors in each redshift bins are assumed to be free parameters, i.e., including M_0 the fitting problem has 12 free parameters in total. With solid black line we show the best fitting three parameter analytic function with the detailed form as specified in the legend. In the *lower panel* $f_{\rm duty}(z)$ is fixed to the above analytic form while the power law indices in each redshift bin $\Gamma(z_i)$ are allowed to vary freely, i.e., this time we have 13 free parameters. Solid black and gray lines show linear and quadratic polynomial approximations to best fitting $\Gamma(z_i)$. The dotted lines and gray shaded regions represent best fit values along with 1σ intervals in case all $\Gamma(z_i)$ and $f_{\rm duty}(z_i)$ are all allowed to be free (19 free parameters).

If the Eddington ratio was independent of redshift and black hole mass, and the latter was proportional to the dark matter halo mass, a simple relation $L_{\rm X} \propto M_{\rm h}$ would obviously hold. In reality, however, the Eddington ratio is determined by the environment of the supermassive black hole. Although the full picture is likely more complex, one can attempt to build a minimalistic model assuming that in the population of AGN, on average, the Eddington ratio is determined by the dark matter halo mass and redshift, $f_{\rm Edd} = f_{\rm Edd}(M_{\rm h}, z)$. Similarly, one can assume that the supermassive black hole mass is also on average determined

Table 1. Best fitting parameter values for Models I and II. Both constrained and unconstrained cases are given.

$f_{\rm duty}(z) = \frac{zc_1^2}{(z-c_2)^2+c_1^2} + c_3$ $M_{\rm h} = M_0 \left(\frac{L_{\rm X}}{L_0}\right)^{c_4+c_5 z+c_6 z^2}$ $L_0 = 10^{41}$ erg/s	Model I ($c_6 \equiv 0$) $+\ f_{\rm duty} \le 1$	Model I ($c_6 \equiv 0$)	Model II $+\ f_{\rm duty} \le 1$	Model II
	best fit	best fit	best fit	best fit
c_1	**0.47**	**0.48**	**0.45**	**0.43**
c_2	**0.83**	**0.94**	**0.80**	**0.90**
c_3	**0.11**	**0.15**	**0.14**	**0.21**
c_4	**0.84**	**0.83**	**0.87**	**0.87**
c_5	**−0.21**	**−0.20**	**−0.28**	**−0.28**
c_6	—	—	**0.023**	**0.023**
$c_7 \equiv \ln M_0$	**27.3**	**27.4**	**27.4**	**27.5**

Table 2. Global performance of various fitting forms.

Model	# param	# dof	χ^2	expected χ^2 (1σ *CL*)
PLE	7	72	96.2	72 ± 12.0
LADE	8	71	67.4	71 ± 11.9
LDDE	9	70	57.8	70 ± 11.8
Model I	6	73	77.2	73 ± 12.1
Model I $+f_{\rm duty} \le 1$	6	73	83.8	73 ± 12.1
Model II	7	72	71.6	72 ± 12.0
Model II $+f_{\rm duty} \le 1$	7	72	77.9	72 ± 12.0

by the halo mass and redshift, $M_{\rm BH} = M_{\rm BH}(M_{\rm h}, z)$, therefore $L_{\rm X} = L_{\rm X}(M_{\rm h}, z)$.

Motivated by these rather trivial and obvious considerations, we will start by assuming that there is a following simple scaling relation between the halo mass and AGN X-ray luminosity

$$M_{\rm h} = M_0 \left(\frac{L_{\rm X}}{L_0}\right)^{\Gamma(z)}, \tag{2}$$

where we take $L_0 = 10^{41}$ erg/s. Having the above scaling relation, we can immediately write for the AGN X-ray LF

$$\frac{{\rm d}n}{{\rm d}L_{\rm X}}(L_{\rm X}, z) = f_{\rm duty}(z) \frac{{\rm d}M_{\rm h}}{{\rm d}L_{\rm X}}(L_{\rm X}, z) \frac{{\rm d}n}{{\rm d}M_{\rm h}}\left[M_{\rm h}(L_{\rm X}, z), z\right], \tag{3}$$

where ${\rm d}n/{\rm d}M_{\rm h}$ is the concordance ΛCDM model halo MF and $f_{\rm duty}$ is the 'duty cycle', in our case defined as a fraction of halos that contain AGN in its active state. For the halo MF we use the analytic form given by Sheth & Tormen (1999) and for the X-ray AGN LF the hard band ($2-10$ keV) measurements from Aird et al. (2010). The Aird et al. (2010) LF data points in nine redshift bins are shown in Fig. 3. We assume that the LF measurements in all the luminosity bins are statistically independent with the errors following Gaussian distribution, i.e., the likelihood function gets factorized and has a simple analytic form. To sample the parametric likelihood function we use Markov chain Monte Carlo (MCMC) methods, in particular Metropolis-Hastings algorithm (Metropolis et al. 1953; Hastings 1970). For finding the maximum likelihood point in parameter space we use downhill simplex method as described in Press et al. (1992).

To gain some idea for the acceptable analytical form for $\Gamma(z)$ and $f_{\rm duty}(z)$ we initially allow these quantities to have free values in all of the redshift bins: $\Gamma(z_i)$, $f_{\rm duty}(z_i)$, $i = 1 \ldots 9$. Thus, including M_0 we have 19 free parameters in total. The dotted lines and gray shaded regions in Fig. 1 show best fit values along with 1σ regions for $\Gamma(z_i)$ and $f_{\rm duty}(z_i)$ obtained from out MCMC calculations. We see that $\Gamma(z_i)$ are quite well fitted by a simple linear form.

As a next step, we fix $\Gamma(z)$ to have a linear redshift dependence $\Gamma(z) = c_4 + c_5 z$ and allow $f_{\rm duty}(z_i)$ to remain free parameters. So our free parameters are: M_0, c_4, c_5, $f_{\rm duty}(z_i)\,(i = 1 \ldots 9)$, i.e. 12 in total. The best fit values for $f_{\rm duty}(z_i)$ are shown with red crosses in the upper panel of Fig. 1. It turns out that these points can be reasonably well approximated with the following analytic form

$$f_{\rm duty}(z) = \frac{c_1^2 z}{(z-c_2)^2 + c_1^2} + c_3\,, \tag{4}$$

i.e., a Lorentzian profile multiplied by z and added a constant offset c_3.[6]

To check for the self-consistency of the above analytic description we now fix $f_{\rm duty}(z)$ to have form as given in Eq. (4), but allow the power law indices in all nine redshift bins to be free parameters, i.e., in this case we have 13 free parameters: M_0, c_1, c_2, c_3, $\Gamma(z_i)\,(i = 1 \ldots 9)$. The best fit values for $\Gamma(z_i)$ are plotted as red crosses in the lower panel of Fig. 1, where with solid lines we also show the best linear and quadratic approximations. Even though the linear approximation for $\Gamma(z)$ seems to capture the redshift dependence of the power law index quite well, quadratic form with its one extra parameter, as it turns out, is statistically well justified.

Thus, our analytic MF to LF mapping is given by Eqs. (3), (2), (4). In the following we call the model with linear (quadratic) $\Gamma(z)$ Model I (Model II). Also, we assume that there is at most one AGN per dark matter halo which is turned on with a probability given by $f_{\rm duty}$, i.e., in that case we have to impose a constraint $f_{\rm duty} \le 1$. However, we also considered unconstrained $f_{\rm duty}$, which can be regarded as a case with more than one AGN per halo. It is interesting that even then $f_{\rm duty}$ does not get much above one (see, e.g., the shaded region in the upper panel of Fig. 1).

In Table 1 we show the best fitting values for all the parameters of Models I and II, with and without additional constraint on $f_{\rm duty}$. The calculated χ^2 values along with expectations are given in Table 2, where we also show the results for pure luminosity evolution (PLE), luminosity and density evolution (LADE), and luminosity dependent density evolution (LDDE) analytic forms taken from Aird et al. (2010). Note that, in order to perform a fair comparison between different analytic fitting forms, we have recalculated

[6] Note that in our earlier paper Hütsi et al. (2012), where we also used the MF to LF mapping in the form of Eq. (3), we had a different analytic form for $f_{\rm duty}(z)$, which turns out to give somewhat poorer fit to the observed LF.

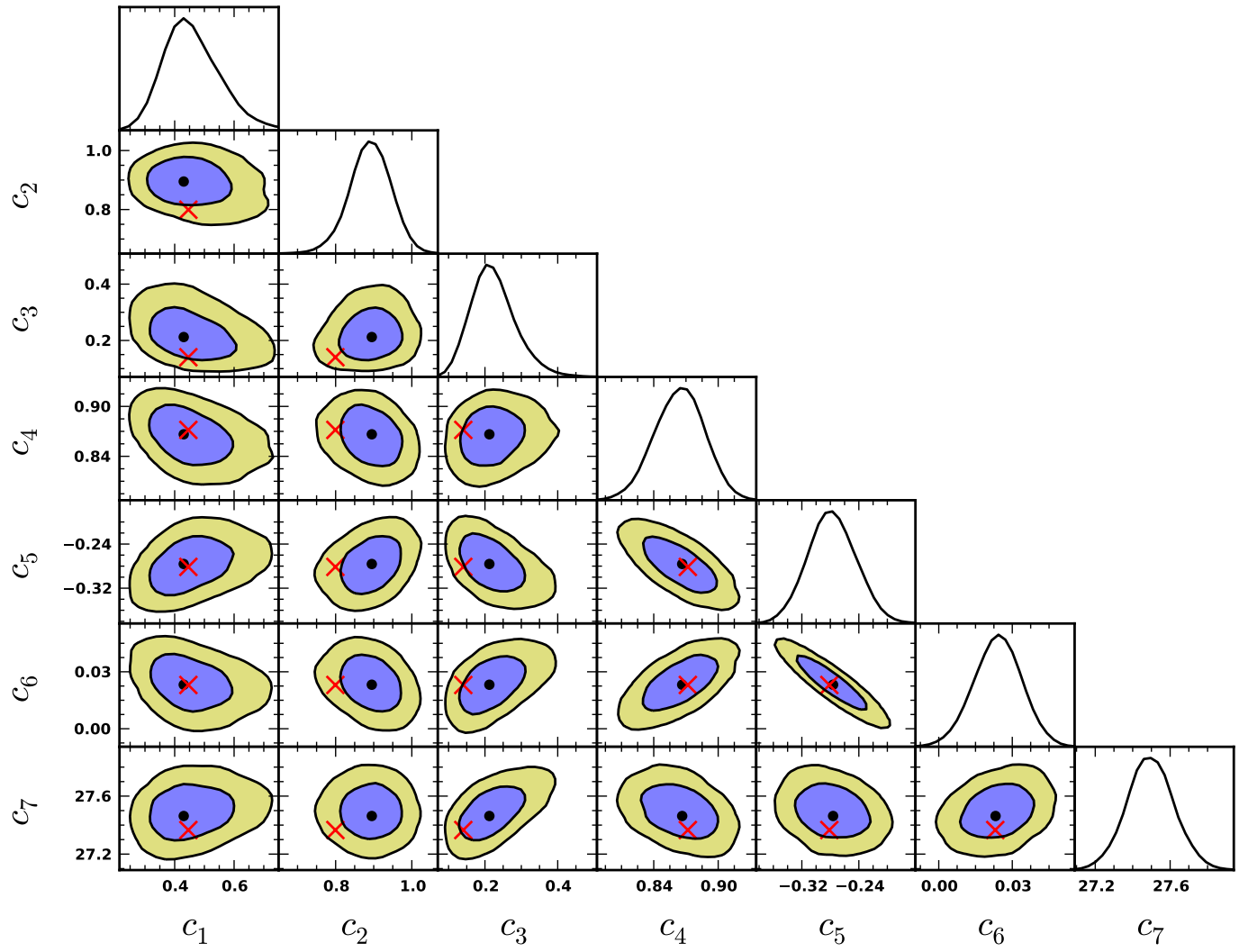

Fig. 2. Marginalized 2D error ellipses representing 1σ and 2σ confidence levels along with 1D marginalized probability distributions (upper panels in each of the columns) for all the free parameters of unconstrained Model II. The black dots and red crosses show the maximum likelihood points for unconstrained and constrained (i.e., $f_{\rm duty} \leq 1$) Model II, respectively.

the best fit models using the same fitting machinery as for our new models. It can be seen that except PLE all of those models provide statistically valid descriptions for the observational data. Even though our MF to LF mapping does not provide as good fit as LADE or LDDE models, it is quite remarkable that this more physical model indeed seems to work. As a benefit, once MF to LF mapping is fixed, our models make several other predictions, which will be discussed in the next section.

As an example of the resulting parameter uncertainties we show in Fig. 2 1σ and 2σ marginalized error regions along with 1D probability distribution functions for all the seven parameters of unconstrained Model II. The black dots and red crosses mark the maximum likelihood points for unconstrained and constrained (i.e., $f_{\rm duty} \leq 1$) cases, respectively. We see that all the model parameters seem to be quite well determined. The strongest degeneracy is seen between parameters c_5 and c_6, which might leave some doubts about the usefulness of the quadratic term in $\Gamma(z)$. However, as seen from the results shown in Table 2, the need for parameter c_6 is statistically well justified, at the confidence level corresponding to $\sim 2.5\sigma$.

In Fig. 3 we plot the LFs in nine redshift bins for the best fitting PLE, LADE, LDDE models, and for our constrained Model II. Original data points with error bars, as determined by Aird et al. (2010), are also shown. Note that our model slightly but systematically overshoots the highest luminosity data point at large redshifts.

3. Implications and shortcomings of the model

In this section we investigate some of the consequences of the MF to LF mapping models presented above.

3.1. Comoving AGN density

We start by investigating the comoving number density of hard band selected X-ray AGN and its dependence on redshift. In the upper panel of Fig. 4 we have plotted comoving number density for three X-ray luminosity intervals as specified in the legend. Here the highest (lowest) group of curves correspond to lowest (highest) luminosities. Along with constrained Model II results for comparison we have also plotted number densities resulting from Ueda et al.

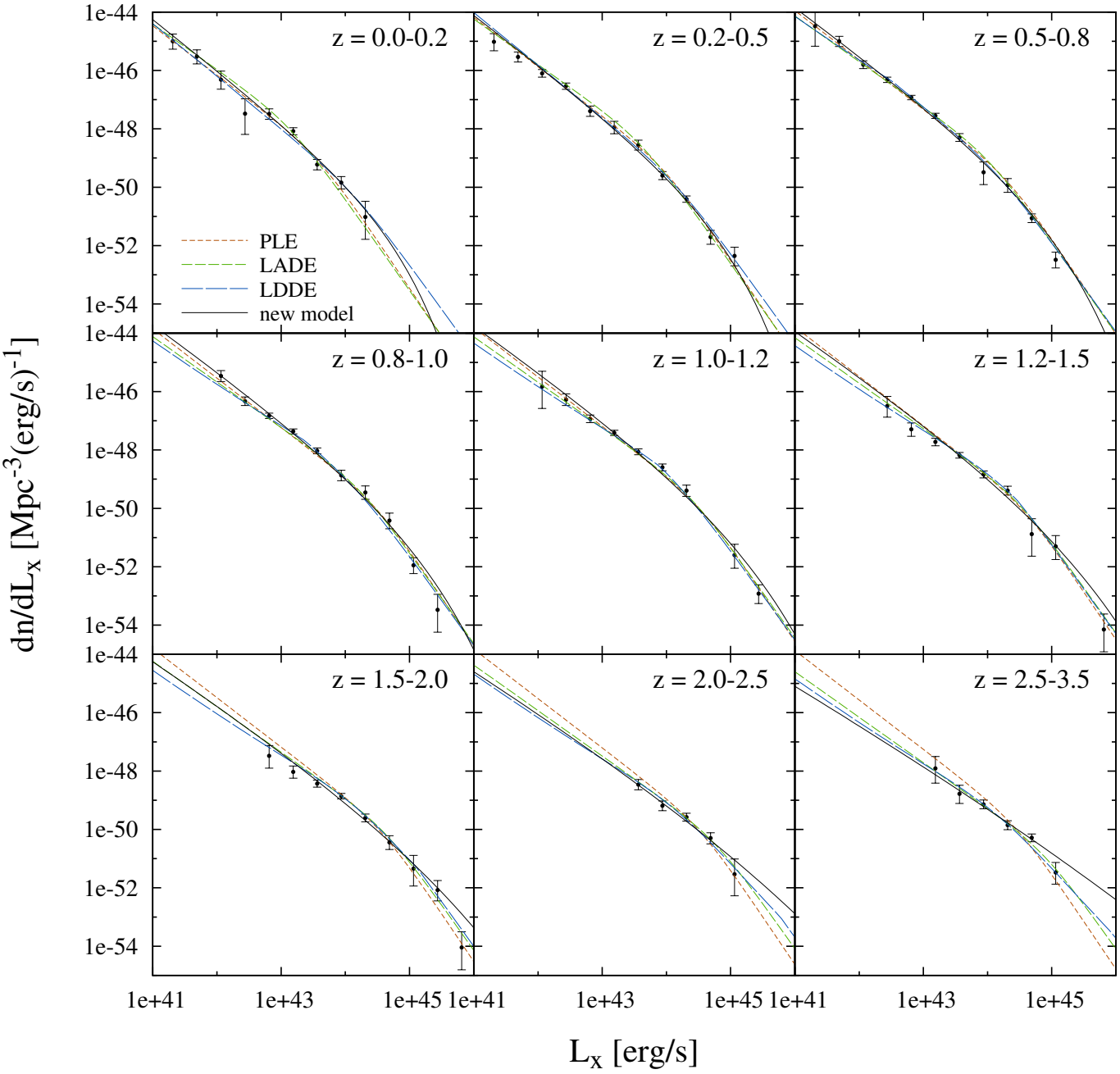

Fig. 3. Best fitting X-ray AGN LFs in nine redshift bins along with observational data from Aird et al. (2010). In addition to our constrained Model II fits we also show the best fitting PLE, LADE and LDDE models with the corresponding analytic forms taken from Aird et al. (2010).

(2003) and Aird et al. (2010) LF fits. In case of Ueda et al. (2003) we have used directly their best fit LF parameters. The comparison of our results with Aird et al. (2010) LDDE parameterization (which as we explained in the previous section was fitted using the same fitting routines as for our new models) should give some idea about the possible level of uncertainty in $n(z)$, since both of the models give statistically valid fits to LF data.

This type of figure is often used to illustrate the anti-hierarchical growth of SMBHs (as manifested by the AGN activity) where the peak in number density moves towards lower redshifts as one considers intrinsically less luminous AGN. However, at least in the case of Aird et al. (2010) LF data, the conclusion about the behavior of the maximum in $n(z)$ curve may depend on the particular choice of the functional form used to fit the X-ray LF data. Indeed, in our LF model, the $n(z)$ maxima for the lowest luminosity bins stay almost at the same position, while for the highest luminosity bin we see gradual movement towards higher redshifts. This does not seem to be entirely incompatible with the pattern of the original LF data points in Fig. 10 in Aird et al. (2010). Furthermore, in our model the rate of change of $n(z)$ has quite strong dependence on luminosity, with the lowest luminosity AGN having the fastest rise in number density going from high redshifts down to $z \sim 1$, the AGN in the intermediate luminosity bin having only very mild increase, the highest luminosity bin show a mild drop in the volume density with the redshift. Note that the

latter is related to the model behavior at large luminosity and redshift, discussed below.

3.2. A possible shortcoming of the model

A careful examination of Fig. 3 reveals that our model overpredicts the numbers of most luminous objects at high redshift (see the three lower panels in Fig. 3). This may point at the shortcoming of the model. Such a shortcoming could be caused by several reasons. One possible cause is the lack of proper treatment of the Eddington luminosity limit. The Eddington ratio analysis later on in this section suggests that this factor may become important in the halo mass range $\log M_{\rm h} \gtrsim 13.5 - 14.5$ at the redshift $z \gtrsim 2 - 3$. It may also be an indication of the shortcoming of the underlying halo mass function, somewhat overpredicting the abundance of massive halos at large redshifts.

Another likely reason may be a failure of the the simple power-law scaling between the luminosity and halo mass, Eq. (2), at large halo masses and large redshifts. Indeed, due to obvious considerations of time available for the black hole growth, the most massive halos at large redshifts may harbor somewhat less massive black holes than implied by Eq. (2). The parameters of the halo mass – luminosity scaling were determined from the global LF fit which is determined by the bulk of the LF data points and is not very sensitive to the data at the extremities as the contribution of high luminosity points to χ^2 is relatively small, due to their small number and also due to their relatively larger uncertainties.

In the conclusion of this discussion we emphasize that the model provides statistically valid global description of the X-ray LF data (Table 2). Its (possible) shortcoming at the high luminosity end affects only a very small number of the most massive halos at large redshifts and does not diminish the overall predictive power of the model for the bulk of typical AGN, as discussed in the following subsections.

3.3. AGN clustering

As our model has fixed a scaling relation between the halo mass and AGN X-ray luminosity, we have immediately definite predictions available for the AGN clustering strength.[7] In the lower panel of Fig. 4 we compare the clustering bias as a function of redshift with the AGN clustering data from Allevato et al. (2011). Allevato et al. (2011) used soft band X-ray data from COSMOS field, which covers 2.13 deg^2 and contains a total of 780 AGN with available redshifts, corresponding to spectroscopic completeness of $\sim 53\%$. In their analysis Allevato et al. (2011) applied a magnitude cut $I_{\rm AB} < 23$ and redshift cut $z < 4$, resulting in 593 objects in their final sample, with effective spectroscopic completeness $\sim 65\%$.

Since the clustering bias in our model depends on AGN luminosity, with more luminous AGN having higher bias parameters, in order to make a fair comparison we have to adjust the effective flux limit appropriately. Since the selection of Allevato et al. (2011) sample was done in the soft band, we have to transform their flux limit to the corresponding limit in the hard band. We do this in a simple way by assuming an effective population-averaged spectral index Γ.[8] The results for four different values of Γ are shown in the lower panel of Fig. 4. As in the hard band one starts to see more and more sources that are obscured in the soft band, the effective spectral index around ~ 1.6 appears to be most appropriate. Considering this, we see that except for the highest redshift bin, our predictions for the bias parameter seem to agree reasonably well with the observational measurements. The highest redshift bin is represented by one point only and it remains to be seen, how significant the deviation is. Also, one has to keep in mind that the measurement of the linear bias parameter, and especially the proper estimation of the errors due to cosmic

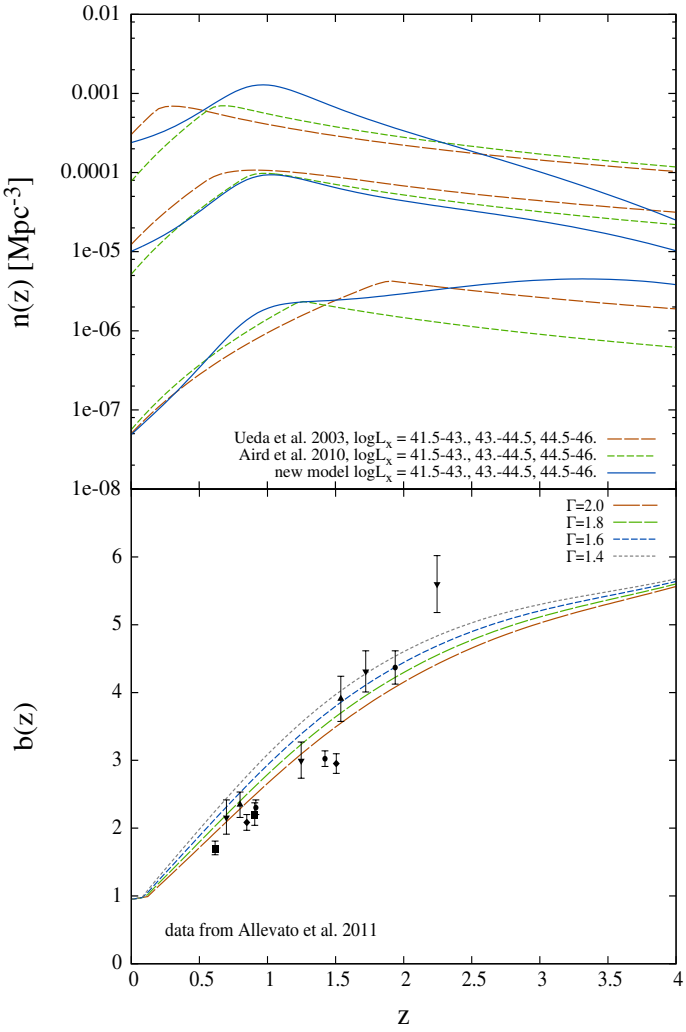

Fig. 4. *Upper panel:* comoving X-ray AGN number densities as a function of redshift for three $2 - 10$ keV band luminosity ranges as shown in the legend. The luminosity is increasing from top to bottom. Along with our constrained Model II we have also plotted the results arising from the LF models of Ueda et al. (2003) and Aird et al. (2010). *Lower panel:* comparison of bias parameters from the constrained Model II with the observational data from Allevato et al. (2011). The four lines assume different effective photon indices ($\Gamma = 1.4, 1.6, 1.8, 2.0$) for the approximate transformation between soft and hard X-ray bands.

[7] In detail, for the halo clustering bias we use the analytical model of Sheth et al. (2001).

[8] Not to be confused with the power law index $\Gamma(z)$ appearing in Eq. (2).

variance (e.g., accidental superclusters in small fields could significantly influence the results) from the fields as small as ~ 2 deg^2 may be quite a cumbersome task.

3.4. AGN duty cycle

In both constrained and unconstrained models the AGN duty cycle (Eq. (3)) peaks at the redshift $z \simeq 1$ (Fig. 1). Although unconstrained models (i.e, when the duty cycle was allowed to take any positive value) result in somewhat better description of the observed X-ray LF data, it is interesting that the peak value of the duty cycle in these models is nevertheless close to unity, with the upper limit of $f_{\rm duty} \lesssim 1.5$ (1σ confidence). This implies that on average there is at most ∼one AGN per dark matter halo. This also implies that the volume densities of dark matter halos and AGN at the redshift $z \sim 1$ match, i.e. there is enough dark matter halos to explain all AGN. In both constrained and unconstrained models the duty cycle drops to $f_{\rm duty} \sim 0.2$ at the redshift $z = 0$ (Fig. 1).

3.5. $M_{\rm h} - L_{\rm X}$ scaling relation

As stated above, the crucial component in our model is the assumption about existence of a scaling relation between the halo mass and AGN X-ray luminosity. Koutoulidis et al. (2012) have recently attempted to infer this type of scaling by using AGN clustering data from several deep X-ray fields: Chandra Deep Field South and North, the AEGIS, the extended Chandra Deep Field South, and the COSMOS field. In Fig. 5 we show their measurements with error bars along with our constrained Model II predictions for redshifts 0.5, 1.0 and 1.5, i.e. approximately covering the redshift range of AGN used in their analysis. The dotted line with surrounding gray band displays the results from the semianalytic galaxy-AGN co-evolution model of Fanidakis et al. (2012) (as presented in Fig. 9 of Koutoulidis et al. (2012)), showing their 'all AGN' case, i.e., the sum of 'hot-halo' and 'starburst' modes. Although the uncertainties are rather large, we see that our model is able to capture the major trend where the more luminous AGN populate preferentially more massive halos. The quantitative agreement between our $M_{\rm h} - L_{\rm X}$ relation and results of Koutoulidis et al. (2012) is truly remarkable as they are based on totally independent arguments.

The long-dashed line in Fig. 5 shows the $M_{\rm h}$-$L_{\rm X}$ scaling one obtains when converting the $M_{\rm h}$-$M_{\rm BH}$ relation of Bandara et al. (2009) by assuming a constant Eddington ratio $f_{\rm Edd} \equiv L_{\rm X}/L_{\rm Edd}(M_{\rm BH})$ of 3×10^{-4}. In reality, as Bandara et al. (2009) $M_{\rm BH}$-$M_{\rm h}$ scaling relation used strong lensing masses derived from the SLACS lens sample with mean redshift $z \simeq 0.2$, we have adjusted the amplitude of the scaling relation to correspond to what one might find at redshifts $z \sim 1$, using results from Croton (2009) semi-analytic models. In Bandara et al. (2009) the authors obtain $M_{\rm BH} \propto M_{\rm h}^{\gamma}$ with $\gamma = 1.55 \pm 0.31$, which agrees quite well with analytic and semi-analytic models of Wyithe & Loeb (2003) and Croton (2009), which provide values $\gamma = 5/3 \simeq 1.67$ and 1.39, respectively. In Croton (2009) and Wyithe & Loeb (2003) models the amplitude of the scaling relation increases by factors of ~ 2 and ~ 4, respectively, while going from $z = 0$ to $z = 1$. However, the power law index γ is independent of redshift in both models.

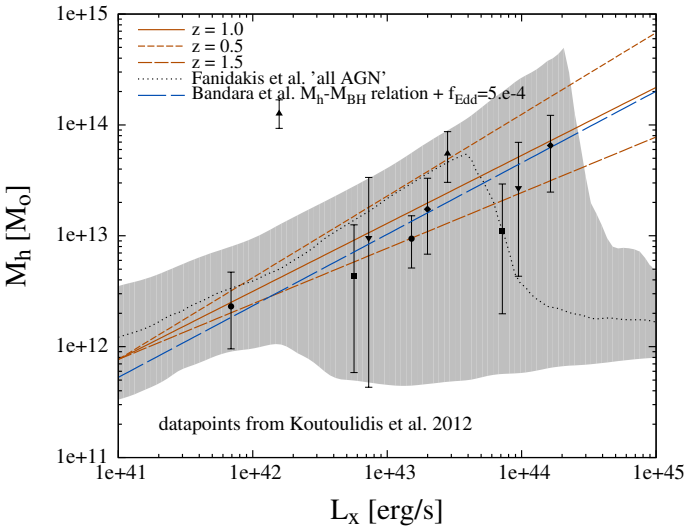

Fig. 5. Comparison of the $M_{\rm h}$-$L_{\rm X}$ scaling relation with the observational data from Koutoulidis et al. (2012). To capture the redshift range of majority of AGN used in Koutoulidis et al. (2012) analysis we have plotted the model scaling relations for three redshifts: $z = 0.5, 1.0, 1.5$. The dotted line with surrounding gray band displays the results from the semianalytic galaxy-AGN co-evolution model of Fanidakis et al. (2012), as presented in Koutoulidis et al. (2012), showing their 'all AGN' case, i.e., the sum of 'hot halo' and 'starburst' modes. The long-dashed line shows the $M_{\rm h}$-$L_{\rm X}$ scaling one obtains once converting the amplitude-adjusted $M_{\rm h}$-$M_{\rm BH}$ relation of Bandara et al. (2009) by using the fixed Eddington ratio $f_{\rm Edd} \equiv L_{\rm X}/L_{\rm Edd}(M_{\rm BH}) = 3 \times 10^{-4}$.

3.6. AGN Black hole masses, Eddington ratios and the growth of SMBHs

By assuming the $M_{\rm BH}$-$M_{\rm h}$ scaling of Bandara et al. (2009) with amplitude adjusted according to Croton (2009) semi-analytic model, we can convert our $L_{\rm X}$-$M_{\rm h}$ relation to $f_{\rm Edd}$-$M_{\rm h}$ scaling relation. This is detailed in Fig. 6 where we have plotted various scalings for five different redshifts. The upper panel gives our results for $L_{\rm X}$-$M_{\rm h}$ with 1σ uncertainties as determined in Section 2 for constrained Model II. The middle panel shows amplitude-adjusted Bandara et al. (2009) $M_{\rm BH}$-$M_{\rm h}$ relation with 1σ uncertainties. In the lower panel we show the Eddington ratios as determined by combining the results from the two uppermost panels. The X-ray luminosities and Eddington ratios refer to the 2–10 keV band and no bolometric corrections were applied. For a typical type I AGN spectrum, the bolometric correction factor should be in the $\sim 5 - 10$ range.

As we can see, the Eddington ratios for high redshift ($z \gtrsim 2$) AGN are predicted to be steeply rising functions of halo mass, while at redshifts $z \sim 1$, i.e. close to the peak in X-ray AGN number density, the dependence of $f_{\rm Edd}$ on $M_{\rm h}$ flattens out, and at lower redshifts the trend is mildly reversed, i.e., the AGN in less massive halos have somewhat higher Eddington ratios. Note that for $z \sim 3$, the 2–10 keV band $f_{\rm Edd}$ reaches values of ~ 0.1 for halo masses $\sim 2 \times 10^{13}\, M_{\odot}$, i.e. the bolometric Eddington ratio will approach ~ 1 at this mass. At larger masses, our $M_{\rm h} - L_{\rm X}$ scaling relation would imply $f_{\rm Edd} \gtrsim 1$. Obviously, this is a consequence of the fact that our $M_{\rm h} - L_{\rm X}$ scaling relation

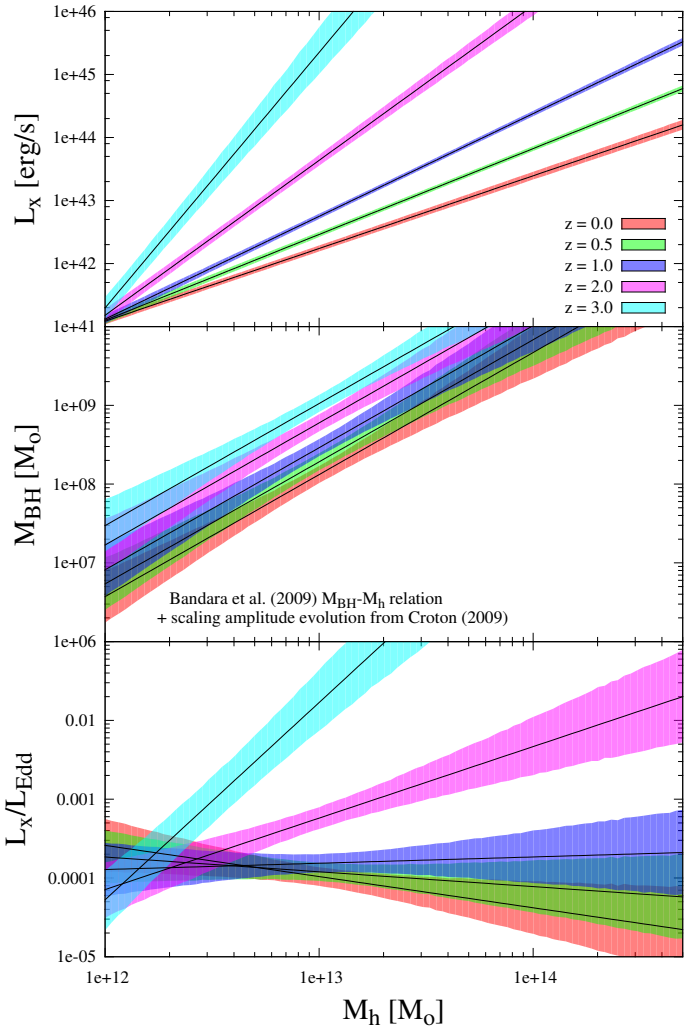

Fig. 6. *Upper panel:* average $L_{\rm X}$-$M_{\rm h}$ relations (Eq. (2)) along with 1σ uncertainties for five different redshifts as given in the legend. *Middle panel:* amplitude-adjusted $M_{\rm BH}$-$M_{\rm h}$ scaling relation with 1σ uncertainty from Bandara et al. (2009). *Lower panel:* Eddington ratios in $2-10$ keV band for five redshifts arising from $L_{\rm X}$-$M_{\rm h}$ and $M_{\rm BH}$-$M_{\rm h}$ relations given in the upper two panels.

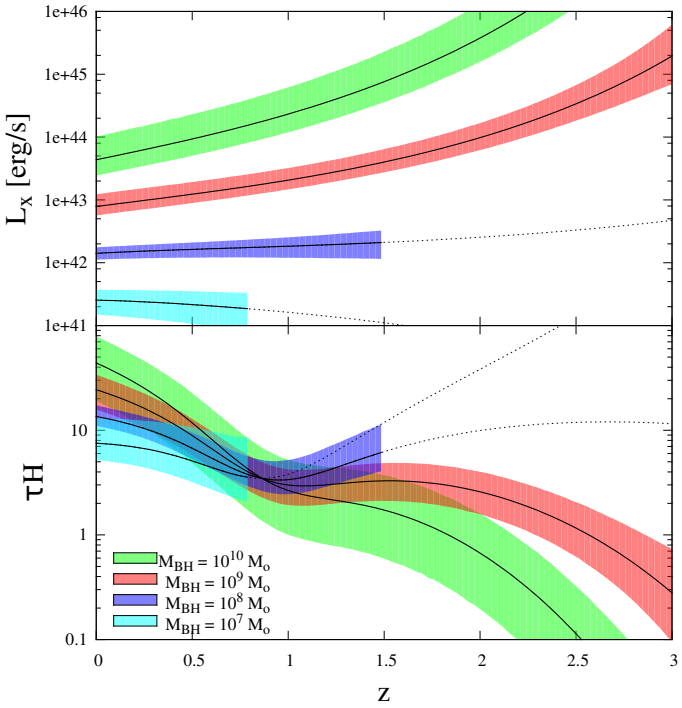

Fig. 7. The hard band X-ray luminosities (*upper panel*) and SMBH e-folding times $\tau \equiv \frac{M_{\rm BH}}{\dot{M}_{\rm BH}}$ in units of the Hubble time (*lower panel*) for various black hole masses as shown in the legend. For the low mass SMBHs at higher redshifts, where they are too faint to be constrained by the observational data, we have shown with dotted lines the extrapolations of the model curves and have omitted the corresponding 1σ uncertainty bands.

does not impose the Eddington luminosity limit. This may be considered as one of the shortcomings of the model, as it was discussed in the section 3.2. One has to note however, that this does not affect overall performance of the model, in the major part of the parameter space. Indeed, so massive halos at redshifts $z \sim 3$ are extremely rare, corresponding to $\sim 4-5\sigma$ peaks in the initial fluctuation field. Bulk of the objects are shining at much smaller Eddington ratios, $\ll 1$.

Having specified $M_{\rm BH}$-$M_{\rm h}$ scaling relation we can also calculate how SMBHs with different masses grow throughout the cosmic time. Taking into account the duty cycle, the population average e-folding time of the SMBH growth is

$$\tau \equiv \frac{M_{\rm BH}}{\dot{M}\, f_{\rm duty}} = \frac{\eta\, M_{\rm BH} c^2}{f_{\rm duty}\, f_{\rm bol}\, L_{\rm X}} \qquad (5)$$

where η is the accretion efficiency, defined as

$$L_{\rm X} = f_{\rm bol}^{-1}\, \eta\, \dot{M} c^2 \qquad (6)$$

$L_{\rm X}$ refers to the X-ray luminosity in the 2–10 keV band used throughout this paper and $f_{\rm bol} \sim 5-10$ is the bolometric correction factor for the 2–10 keV band. The e-folding time can be further expressed though the Eddington ratio:

$$\tau = \frac{\eta\, M_{\rm BH} c^2}{f_{\rm duty}\, f_{\rm bol}\, f_{\rm Edd}\, L_{\rm Edd}} = 0.45\, \frac{\eta}{f_{\rm duty}\, f_{\rm bol}\, f_{\rm Edd}}\ {\rm Gyrs} \qquad (7)$$

In the lower panel of Fig. 7 we plot the e-folding time in units of the Hubble time, i.e. $\tau H(z)$, vs redshift for several values of the black hole mass. Shown in the upper panel is the evolution of the population average $2-10$ keV band X-ray luminosity with redshift. AGN harboring black holes with masses less than a $\sim$few$\times 10^8\, M_\odot$ are too faint at large redshifts and fall outside the luminosity range of the X-ray LF data of Aird et al. (2010) used in this study. Therefore they are not directly constrained by the X-ray data. At these redshifts we only show with dotted lines the extrapolations of the central model curves and omit the 1σ uncertainty regions.

We see that the X-ray luminosity of more massive SMBHs declines faster with the redshift than for less massive ones. For $\sim 10^8\, M_\odot$ black holes $L_{\rm X}$ stays almost constant while for even lower mass SMBHs the evolutionary trend is slightly reversed, i.e., the objects are getting somewhat brighter as one moves towards lower redshifts. As one might have expected from the results plotted in the bottom panel of Fig. 6, for the typical X-ray selected AGN the corresponding SMBH e-folding times are large in comparison to the Hubble time. With the exception of most massive

SMBHs at large redshifts, the typical X-ray selected AGN are not in the rapid mass growth regime in the $z \sim 0-3$ redshift range.

Note that the crossing of the model curves in the lower panel of Fig. 7 at the redshift of $z \sim 0.85$ is artificial and does not seem to have any physical meaning. It is driven by the equality of the power law indices of the $M_{\rm BH}$-$M_{\rm h}$ and $M_{\rm h} - L_{\rm X}$ scaling relations, which leads to the τH being independent of $M_{\rm BH}$ at that particular z.

Thus, with the particular form of the $M_{\rm BH}$-$M_{\rm h}$ scaling relation from Bandara et al. (2009) with amplitude evolution from Croton (2009), our model implies relatively low Eddington ratios, $f_{\rm Edd} \sim 10^{-4} - 10^{-3}$. In the redshift range $z \sim 0-3$, for a typical X-ray selected AGN accretion proceeds in the 'hot halo mode' characterized by relatively low mass accretion rate and large e-folding time for SMBH mass growth. Obviously, this conclusion critically depends on the assumed $M_{\rm BH}$-$M_{\rm h}$ scaling relation. Indeed, as X-ray luminosity for the given halo mass is directly determined by our model from the $L_X - M_h$ mapping, the Eddington ratio scales inversely with the black hole mass, while e-folding time is linearly proportional to the black hole mass.

4. Conclusions

Even though dark matter halos are highly nonlinear objects, with the aid of cosmological N-body simulations along with heuristic analytic models, one has obtained a very good knowledge about their redshift dependent MF and clustering bias. Since in CDM type cosmologies, where the structure forms according to the 'bottom-up' scenario, it is quite natural to assume that the buildup of more massive object has also been accompanied by the formation of more massive SMBH in its center. This is also manifested on average by a more luminous AGN. Despite the fact that there are certainly several other key parameters beyond the halo mass, which influence the central SMBH mass, $M_{\rm h}$ is surely expected to be one of the main contributors.

In this paper, we assumed that a scaling relation between X-ray AGN luminosity and its host halo mass does exist. Assuming further that the dark matter halo mass function is described by the concordance ΛCDM model, we can predict X-ray AGN luminosity function. Comparing the latter with the redshift dependent AGN X-ray luminosity function known from observations we can determine the shape and parameters of the $M_{\rm h} - L_{\rm X}$ scaling relation.

Our main conclusions are the following:

- We have shown that a simple scaling relation in the form of Eq. (2), where $\Gamma(z)$ is a linear or quadratic polynomial, allows one to obtain X-ray AGN LFs consistent with observational data. The best fitting model parameters along with χ^2 values are summarized in Tables 1 and 2.
- Since the $M_{\rm h}$-$L_{\rm X}$ scaling establishes a link to the halo MF, our model is certainly more predictive compared to the usual specifically tailored multi-parameter fitting forms to the X-ray LF data. In particular, our model predicts the redshift and luminosity dependence of the X-ray AGN clustering bias, which is in reasonable agreement with observational data.
- Our $M_{\rm h}$-$L_{\rm X}$ scaling relation is in good agreement with the data presented in Koutoulidis et al. (2012), and with semianalytic galaxy-AGN co-evolution models of Fanidakis et al. (2012). Comparison with semianalytical models suggests that for X-ray AGN the dominant accretion mode is the 'hot halo mode', in contrast to the 'starburst mode' which is compatible of being dominant accretion mode for somewhat less clustered but more energetic quasars.
- Our model also includes AGN duty cycle. It peaks at the redshift $z \simeq 1$ and its value at the peak is consistent with unity, implying that there is at most one AGN per dark matter halo.
- We further combined our $M_{\rm h}$-$L_{\rm X}$ relation with $M_{\rm h}$-$M_{\rm BH}$ relation from Bandara et al. (2009), along with its redshift evolution taken from Croton (2009), and obtained Eddington ratios $f_{\rm Edd} \equiv L_{\rm X}/L_{\rm Edd} \sim 10^{-4} - 10^{-3}$ (2–10 keV band, no bolometric correction applied). This result presents another evidence that at the redshifts below $z \lesssim 3$, SMBHs in X-ray selected AGN typically grow through 'hot halo' accretion mode characterized by low mass accretion rate and large e-folding time. It is also consistent with the fact that according to their clustering strengths, X-ray selected AGN populate group-sized dark matter halos and thus are typically embedded in hot gaseous halos.

Appendix A: Analytic fits for concordance ΛCDM halo MF and bias parameters

To facilitate a fast check of our results for those who do not have numerical routines for the halo MF and clustering bias available, we provide here analytic fits for those quantities, valid for the mass and redshift ranges relevant for this study: $M_{\rm h} \gtrsim 10^{12}\,M_\odot$, $z < 3-4$.

Halo MF can be approximated as

$$\frac{{\rm d}n}{{\rm d}M_{\rm h}}(M_{\rm h}, z) \simeq A(z) \left(\frac{M_{\rm h}}{M_*(z)}\right)^{\alpha(z)} \exp\left[-\left(\frac{M_{\rm h}}{M_*(z)}\right)^{\beta(z)}\right],$$

where

$$\begin{aligned} A(z) &= \exp\left(-0.1057 \cdot z^2 + 2.677 \cdot z - 43.89\right), \\ M_*(z) &= \exp\left(0.08305 \cdot z^2 - 1.709 \cdot z + 33.17\right), \\ \alpha(z) &= 0.007189 \cdot z^2 - 0.1692 \cdot z - 1.919, \\ \beta(z) &= 0.001109 \cdot z^2 - 0.04119 \cdot z + 0.7188. \end{aligned}$$

Similarly, for the halo clustering bias, as a function of halo mass and redshift, one approximately obtains

$$b(M_{\rm h}, z) \simeq c_1(M_{\rm h}) \cdot z^2 + c_2(M_{\rm h}) \cdot z + c_3(M_{\rm h}),$$

where

$$\begin{aligned} c_1(M_{\rm h}) &= \exp\left[0.01703 \ln(M_{\rm h})^2 - 0.6629 \ln(M_{\rm h}) + 3.566\right], \\ c_2(M_{\rm h}) &= \exp\left[0.01495 \ln(M_{\rm h})^2 - 0.5196 \ln(M_{\rm h}) + 1.630\right], \\ c_3(M_{\rm h}) &= \exp\left[0.02866 \ln(M_{\rm h})^2 - 1.534 \ln(M_{\rm h}) + 20.38\right]. \end{aligned}$$

Under the mass and redshift constraints as given above, those analytic forms provide fits to the Sheth & Tormen (1999) MF and Sheth et al. (2001) bias parameter with accuracies $\sim 10\%$ and better than 5%, respectively. NOTE that in the above formulae we have assumed that MF is measured in units of $h^3{\rm Mpc}^{-3}/h^{-1}M_\odot$ and halo mass in $h^{-1}M_\odot$, while in the main part of our paper we fixed the reduced Hubble parameter to $h = 0.7$.

Acknowledgements. We thank James Aird for providing us the tables of hard band X-ray luminosity function measurements.

References

Aird, J., Nandra, K., Laird, E. S., et al. 2010, MNRAS, 401, 2531
Alexander, D. M., Bauer, F. E., Brandt, W. N., et al. 2003, AJ, 126, 539
Allevato, V., Finoguenov, A., Cappelluti, N., et al. 2011, ApJ, 736, 99
Bandara, K., Crampton, D., & Simard, L. 2009, ApJ, 704, 1135
Brandt, W. N. & Hasinger, G. 2005, ARA&A, 43, 827
Coil, A. L., Georgakakis, A., Newman, J. A., et al. 2009, ApJ, 701, 1484
Comastri, A., Ranalli, P., Iwasawa, K., et al. 2011, A&A, 526, L9
Croton, D. J. 2009, MNRAS, 394, 1109
Fanidakis, N., Baugh, C. M., Benson, A. J., et al. 2012, MNRAS, 419, 2797
Ferrarese, L. 2002, ApJ, 578, 90
Ferrarese, L. & Ford, H. 2005, Space Sci. Rev., 116, 523
Gandhi, P., Garcet, O., Disseau, L., et al. 2006, A&A, 457, 393
Gilli, R., Zamorani, G., Miyaji, T., et al. 2009, A&A, 494, 33
Hasinger, G., Miyaji, T., & Schmidt, M. 2005, A&A, 441, 417
Hastings, W. 1970, Biometrika, 97
Hütsi, G., Gilfanov, M., & Sunyaev, R. 2012, A&A, 547, A21
Kolodzig, A., Gilfanov, M., Hütsi, G., & Sunyaev, R. 2013, in preparation
Kolodzig, A., Gilfanov, M., Sunyaev, R., Sazonov, S., & Brusa, M. 2012, arXiv:1212.2151
Kormendy, J. & Bender, R. 2011, Nature, 469, 377
Kormendy, J. & Richstone, D. 1995, ARA&A, 33, 581
Koutoulidis, L., Plionis, M., Georgantopoulos, I., & Fanidakis, N. 2012, MNRAS, 101
Merloni, A., Predehl, P., Becker, W., et al. 2012, eROSITA Science Book: Mapping the Structure of the Energetic Universe
Metropolis, N., Rosenbluth, A. W., Rosenbluth, M. N., Teller, A. H., & Teller, E. 1953, Journal of Chemical Physics, 21, 1087
Murray, S. S., Kenter, A., Forman, W. R., et al. 2005, ApJS, 161, 1
Predehl, P., Andritschke, R., Böhringer, H., et al. 2010, in Society of Photo-Optical Instrumentation Engineers (SPIE) Conference Series, Vol. 7732, Society of Photo-Optical Instrumentation Engineers (SPIE) Conference Series
Press, W. H., Teukolsky, S. A., Vetterling, W. T., & Flannery, B. P. 1992, Numerical recipes in FORTRAN. The art of scientific computing
Sheth, R. K., Mo, H. J., & Tormen, G. 2001, MNRAS, 323, 1
Sheth, R. K. & Tormen, G. 1999, MNRAS, 308, 119
Ueda, Y., Akiyama, M., Ohta, K., & Miyaji, T. 2003, ApJ, 598, 886
Wyithe, J. S. B. & Loeb, A. 2003, ApJ, 595, 614
Xue, Y. Q., Luo, B., Brandt, W. N., et al. 2011, ApJS, 195, 10